EDI

An X-ray scattering and electron microscopy study of methylammonium bismuth perovskites for solar cell applications

Chan Kyu Kwak
Department of Chemical and Biological Engineering, The University of Sheffield, Sheffield S1 3JD, U.K.

Alex T. Barrows
Department of Physics & Astronomy, The University of Sheffield, Sheffield S3 7RH, U.K.

Andrew J. Pearson
Optoelectronics Group, Cavendish Laboratory, Cambridge CB3 0HE, U.K.

David G. Lidzey
Department of Physics & Astronomy, The University of Sheffield, Sheffield S3 7RH, U.K.

Alan D.F. Dunbar[a)]
Department of Chemical and Biological Engineering, The University of Sheffield, Sheffield S1 3JD, U.K.

(Received 11 October 2016; accepted 6 December 2016)

Photovoltaics made from organic–inorganic hybrid perovskite semiconductors are attracting significant interest due to their ability to harvest sunlight with remarkable efficiency. The presence of lead in the best performing devices raises concerns regarding their toxicity, a problem that may create barriers to commercialization. Hybrid perovskites with reduced lead content are being investigated to overcome this issue and here we evaluate bismuth as a possible lead substitute. For a series of hybrid perovskite films with the general composition $CH_3NH_3(Pb_yBi_{1-y})I_{3-x}Cl_x$, we characterize their optical and structural properties using UV–Vis spectroscopy, scanning electron microscopy and grazing incidence wide angle X-ray scattering. We show that they form crystalline structures with an optical band gap, around 2 eV for $CH_3NH_3BiI_3$. However, preliminary solar cell tests show low power conversion efficiencies (<0.01%) due to both incomplete precursor conversion and material de-wetting from the substrate. The overall outcome is severely limited photocurrent. With current processing methods the general applicability of hybrid bismuth perovskites in photovoltaics may be limited.

I. INTRODUCTION

The abundance of sunlight makes it a highly attractive source of green energy. Within the area of photovoltaic (PV) technologies, silicon is the dominant technology due to its mature manufacturing methods and moderate processing costs.[1] Recently, hybrid perovskite photovoltaics have attracted great interest due to their outstanding efficiency, a composition that is based on inexpensive materials and their ease of fabrication.[2–7] As a consequence of these promising characteristics, hybrid perovskites are showing strong potential to drive the next wave of widespread PV adoption; both in areas currently dominated by silicon and in innovative applications such as building integrated PV.

The term 'perovskite' can be used to describe a crystalline material with the general chemical formula ABX_3. Hybrid perovskites are so named because the A cation is organic, with common examples in the area of solar cell research including methylammonium ($CH_3NH_3^+$) and formamidinium ($HC(NH_2)_2^+$).[6,7] These materials typically employ Pb as the B cation, with halides such as Cl, I, and Br used as the X anion. Since 2009 organo-lead halide perovskites have become pioneer materials in the development of next-generation PV,[8–11] with initial power conversion efficiencies (PCEs) now standing at 22% for laboratory scale devices.[12] Among the challenges facing the scale-up of perovskite PV, the toxicity of the semiconductors has been raised as a potential issue owing to the presence of lead.[13,14] Specifically, beyond the hazards present during solar cell fabrication and end-of-life recycling, the ability to deploy such cells in real world applications may be prohibited by the potential risk for lead seepage that occurs due to encapsulation failure (the solubility of organo-lead halide perovskites in water has been well-documented).[15] To overcome this, research into reduced lead or lead-free perovskites has gained traction over the past few years and amongst the possible substitute metals tin has showed reasonable promise.[11,16,17] Notable highlights include the demonstration of $CH_3NH_3SnI_3$ solar cells with an initial PCE above

Contributing Editor: Chris Nicklin
[a)]Address all correspondence to this author.
e-mail: a.dunbar@sheffield.ac.uk
DOI: 10.1557/jmr.2016.499

6%,[11] however the efficient photovoltaic functionality of Sn rich phases in mixed Sn/Pb perovskites has been questioned.[16] Additional issues that include semiconductor oxidation and the mitigation of hysteresis effects in devices continues to drive the development of reduced lead perovskites with the ultimate goal of matching the performance characteristics of the original lead-based semiconductors. Another study considered other metals that match the requirements on electron valency and size tolerance within the perovskite lattice.[18] To reduce the use of lead, Park et al. have introduced bismuth as substitute for lead.[19] Bismuth has much lower toxicity than lead and they found that caesium-bismuth perovskite showed a PCE of 1.09%, however, Cs is still considered mildy toxic. They also reported methylammonium Bi-perovskite which to which they assigned a $MA_3Bi_2I_9$ structure and measured a PCE of 0.12%. Slavney et al. studied a double-perovskite structure $Cs_2Ag^+Bi^{3+}Br_6$ finding lattice a unit-cell axis of 11.25 Å is roughly double than that of $(MA)PbBr_3$, however they did not test any photovoltaic devices.[20]

Herein we explore the use of bismuth as a low toxicity alternative to lead in hybrid perovskite semiconductors. Alongside a control sample of $CH_3NH_3PbI_{3-x}Cl_x$ we investigate a range of perovskites with the composition $CH_3NH_3(Pb_yBi_{1-y})I_{3-x}Cl_x$ where y varies between 0 and 1 and x is small, with such samples prepared from a range of precursors (including $BiCl_3$ and BiI_3) and precursor blend ratios. Our study places particular focus on the crystallinity and phase purity of each perovskite, with scanning electron microscopy (SEM), energy-dispersive X-ray spectroscopy (EDS), and grazing incidence wide angle X-ray scattering (GIWAXS) measurements used to characterize their nanoscale structure and composition. Although their initial performance in solar cell devices is not promising, our structural data helps us to understand why this is the case. In general our results provide important insight into the processability of bismuth perovskites, thereby helping to refine the choice of materials and processing methods used for developing high performance hybrid perovskites with low toxicity.

The presentation of our results proceeds as follows. We first consider the linear UV–Vis absorption spectra of each perovskite sample, before discussing composition and microstructure characteristics in depth via SEM, EDS, and GIWAXS analysis. This data is used to build a preliminary model regarding the formation process for bismuth perovskites, in addition to providing insight into the ability for binary-metal compositions (i.e., Pb/Bi mixtures) to form crystalline semiconductor structures of high phase purity. Lastly, the results from an initial solar cell device study are presented. Our study concludes by considering engineering strategies for improving bismuth perovskite film quality.

II. RESULTS AND DISCUSSION

The general route for preparing hybrid perovskites films involves the coordination of an organic cation within a metal-halide lattice structure. This process can take place in solution, or via thermal annealing of a precursor film with an appropriate starting stoichiometry (i.e., relative concentrations of organic and inorganic material). To synthesize organo-bismuth halide perovskites, CH_3NH_3I (methylammonium iodide, hereafter referred to as MAI), BiI_3 and $BiCl_3$ were used as precursor materials to form $CH_3NH_3BiI_3$ and $CH_3NH_3BiI_{3-x}Cl_x$. The role of starting stoichiometry for the pure tri-iodide perovskite $CH_3NH_3BiI_3$ was investigated by considering 1:1 or 3:1 mol% mixtures of MAI and BiI_3 respectively. Finally, The precursors for $CH_3NH_3BiI_{3-x}Cl_x$ and $CH_3NH_3PbI_{3-x}Cl_x$ were mixed to form three mixed metal cation perovskites with nominal compositions $CH_3NH_3(Pb_{0.25}Bi_{0.75})I_{3-x}Cl_x$, $CH_3NH_3(Pb_{0.5}Bi_{0.5})I_{3-x}Cl_x$ and $CH_3NH_3(Pb_{0.75}Bi_{0.25})I_{3-x}Cl_x$. A total of seven perovskite samples are considered in this study, with full preparation details provided in the experimental methods.

A. UV–Vis absorption

Figure 1 shows the UV–Vis absorption spectra for each perovskite film, where it can be seen that each sample exhibits a relatively strong absorption peak centered around 500 nm. For our control sample $CH_3NH_3PbI_{3-x}Cl_x$, its optical absorption extend to long wave length >750 nm where there is a distinct edge which when extrapolated meets the x-axis at approximately 820 nm, equating to a band gap of 1.51 eV in reasonable agreement

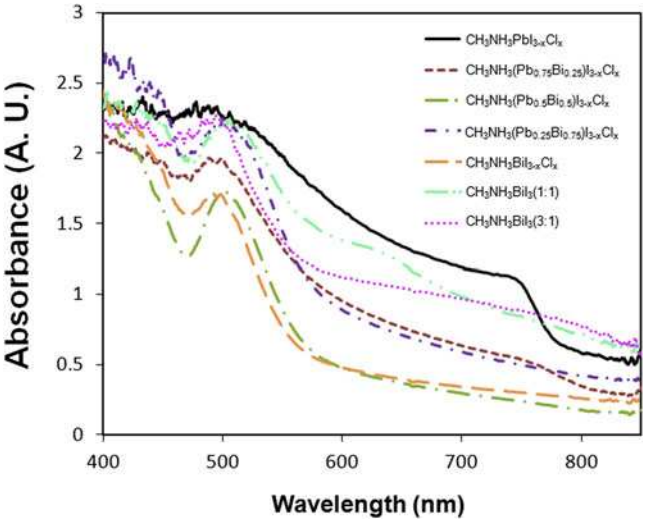

FIG. 1. Absorbance spectra of $CH_3NH_3PbI_{3-x}Cl_x$, $CH_3NH_3BiI_{3-x}Cl_x$, $CH_3NH_3BiI_3$ (1:1), $CH_3NH_3BiI_3$ (3:1), $CH_3NH_3(Pb_{0.25}Bi_{0.75})I_{3-x}Cl_x$, $CH_3NH_3(Pb_{0.5}Bi_{0.5})I_{3-x}Cl_x$ and $CH_3NH_3(Pb_{0.75}Bi_{0.25})I_{3-x}Cl_x$ films prepared on glass substrates. Precursor samples were annealed at 90 °C for 90 min to form each perovskite. (color online)

with earlier reports.[6,21] This is close to the value reported for $CH_3NH_3PbI_3$,[22,23] again suggesting the low/trace levels of Cl in this perovskite. Among the mixed metal perovskites only $CH_3NH_3(Pb_{0.75}Bi_{0.25})I_{3-x}Cl_x$ showed a weaker absorption shoulder in the near-IR region of the light spectrum, at a wave length similar to that observed for the control sample (>750 nm). We tentatively attribute this feature to the presence of pure lead perovskite phases within the sample, given the 3× difference in lead molar content compared to bismuth in the precursor. Further increases in bismuth content within the sample, from $Pb_{0.75}Bi_{0.25}$ to $Pb_{0.25}Bi_{0.75}$, results in the eventual disappearance of this feature. For the pure bismuth perovskites, $CH_3NH_3BiI_3$ (1:1) prepared from a 1:1 precursor stoichiometry shows a weak absorption edge at approximately 645 nm, whereas $CH_3NH_3BiI_3$ (3:1) prepared from a 3:1 precursor stoichiometry and $CH_3NH_3BiI_{3-x}Cl_x$ do not. For $CH_3NH_3BiI_{3-x}Cl_x$ we estimate an optical band gap of 2.1 eV via extrapolation of the absorption edge beyond 510 nm. Note however that this method does not readily extend to every perovskite considered here, as the slow and incomplete drop-off in absorption (likely an indication of pronounced light scatter) will introduce unintended artifacts.[24]

B. SEM/EDS characterization

To study in detail the microstructure of each perovskite film, in addition to confirming their composition, we recorded a series of SEM images and EDS chemical surveys. Figure 2 shows representative SEM images for each perovskite. From Fig. 2(a), which corresponds to our control sample, it can be seen that $CH_3NH_3PbI_{3-x}Cl_x$ consists of a relatively dense distribution of elongated crystals, each having a characteristic length between 3 and 10 μm. Quantitative analysis of this image suggests a surface coverage of 74%. For the mixed metal perovskites, shown here in Figs. 2(b)–2(d), two distinct structure types are present; a compact distribution of

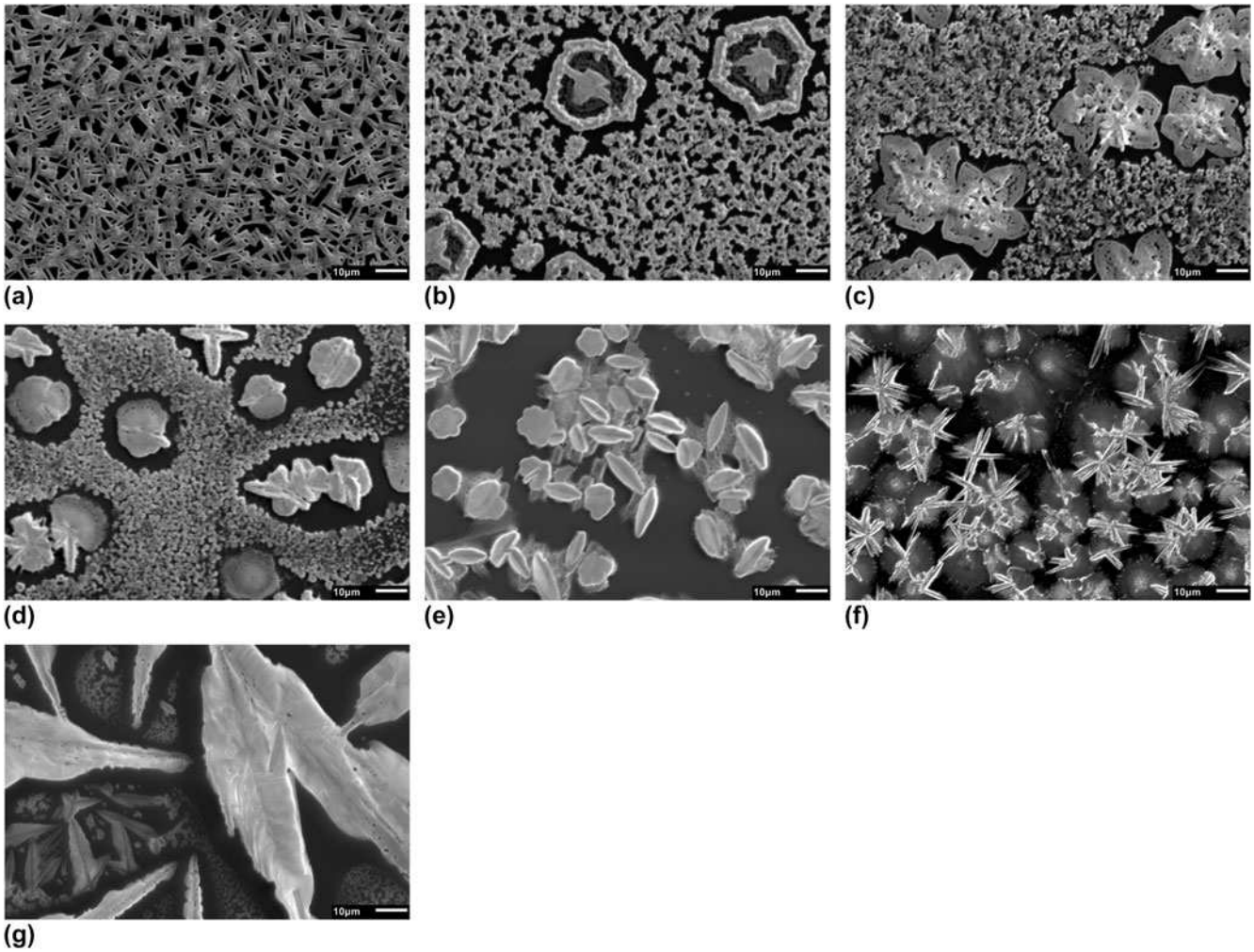

FIG. 2. SEM images of (a) $CH_3NH_3PbI_{3-x}Cl_x$, (b) $CH_3NH_3(Pb_{0.75}Bi_{0.25})I_{3-x}Cl_x$, (c) $CH_3NH_3(Pb_{0.5}Bi_{0.5})I_{3-x}Cl_x$, (d) $CH_3NH_3(Pb_{0.25}Bi_{0.75})I_{3-x}Cl_x$, (e) $CH_3NH_3BiI_{3-x}Cl_x$, (f) $CH_3NH_3BiI_3$ (1:1), and (g) $CH_3NH_3BiI_3$ (3:1) films prepared on silicon substrates. Scale bar corresponds to 10 μm.

micron-sized crystallites that cover a sizable fraction of the substrate, and dispersed structures with a size between 20 and 30 μm. Note that these relatively large features are often surrounded by a region void of any material, suggesting that mass transport and/or substrate de-wetting has taken place during their formation.[25] In general, these structures are present in greater number when the relative concentration of Bi in the sample increases. Although this might suggest the presence of separate perovskite phases in the sample (i.e., regions of pure $CH_3NH_3PbI_{3-x}Cl_x$ that are spatially distinct from regions of pure $CH_3NH_3BiI_{3-x}Cl_x$), EDS mapping indicates that the distribution of Bi throughout the sample is reasonably uniform (data presented in the Supplementary Material). As a consequence we suggest that the formation of either crystallite structure is not determined primarily by metal content, and is instead governed by factors that include halide composition, the dynamics of precursor conversion and the local presence of defects/impurities in the sample that act as possible nucleation sites for crystal formation.

The SEM image for $CH_3NH_3BiI_{3-x}Cl_x$ is shown in Fig. 2(e). Here it can be seen that multiple 'flower' shaped features are present, many of which appear to sit edge on from the substrate surface. These features are often surrounded by regions of what appears to be less structured material, however their total surface coverage is low (c. 50%). In Fig. 3(f) the film corresponding to $CH_3NH_3BiI_3$ (1:1) shows a mixture of short needle like crystals protruding from central points (about 10 μm long) sitting on top of round unstructured regions that are between 10 and 35 μm in diameter. For this sample the total surface coverage is much higher than for $CH_3NH_3BiI_{3-x}Cl_x$. The $CH_3NH_3BiI_3$ (3:1) perovskite film is principally characterized by large crystals (>50 μm in length) alongside local regions containing smaller structures as shown in Fig. 2(g). Connectivity between these regions is however poor, with many areas of the substrate containing no material whatsoever.

Having established that the bismuth perovskite films are comprised of multiple crystal structures with characteristically distinct sizes, we proceed to discuss their chemical composition as determined by EDS mapping. Table I summarizes the results of these measurements, where values correspond to the stoichiometric ratio of each element. Corresponding images are presented in the Supplementary Material Figs. S1–S7. As reported previously, Cl was almost completely absent in the $CH_3NH_3PbI_{3-x}Cl_x$ film,[26] indicating its removal from the sample during processing (i.e., via sublimation with excess MAI)[27–29] or its preferential location at the substrate interface. As the ratio of Bi is increased in the mixed metal perovskite the Cl content rises from 0.46 (25% Bi) up to 1.47 (100% Bi). Spatially averaged

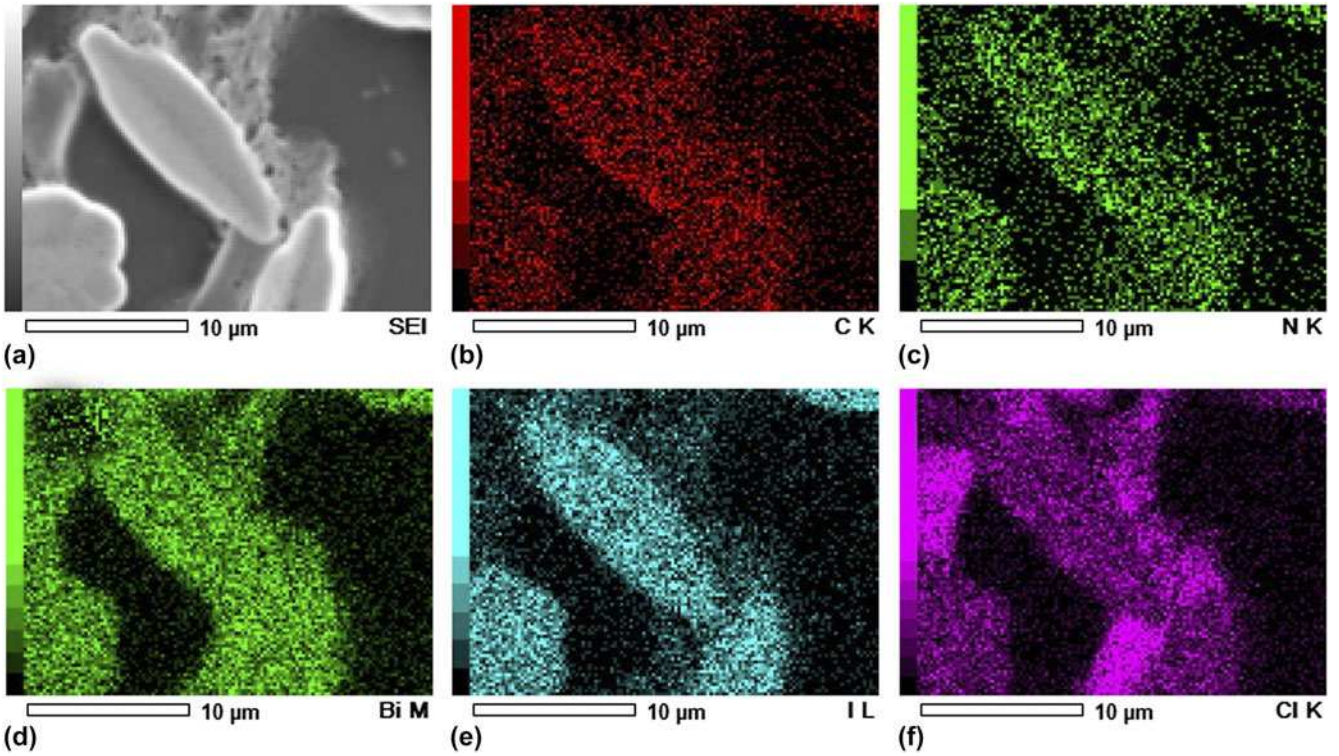

FIG. 3. SEM image of (a) $CH_3NH_3BiI_{3-x}Cl_x$ and corresponding EDS analysis with elemental mapping of (b) carbon, (c) nitrogen, (d) bismuth, (e) iodine, and (f) chlorine. (color online)

TABLE I. The stoichiometric ratio of elements as determined by EDS for the $CH_3NH_3PbI_{3-x}Cl_x$, mixed metal perovskites, $CH_3NH_3BiI_xCl_y$, and $CH_3NH_3BiI_x$ films as determined by EDS. The numbers in parenthesize correspond to the target stoichiometric ratio determined by the composition of the precursor solutions used.

Materials	C	N	Pb	Bi	I	Cl
$CH_3NH_3PbI_{3-x}Cl_x$	3.12 (1)	0.33 (1)	1 (1)	...	2.58 (3−x)	0.03 (x)
$CH_3NH_3Pb_{0.75}Bi_{0.25}I_{3-x}Cl_x$	2.96 (1)	0.55 (1)	0.72 (0.75)	0.28 (0.25)	2.76 (3.5−x)	0.46 (x)
$CH_3NH_3Pb_{0.5}Bi_{0.5}I_{3-x}Cl_x$	2.59 (1)	0.72 (1)	0.38 (0.50)	0.62 (0.50)	2.94 (3.5−x)	0.76 (x)
$CH_3NH_3Pb_{0.25}Bi_{0.75}I_{3-x}Cl_x$	2.61 (1)	0.97 (1)	0.26 (0.25)	0.74 (0.75)	2.5 (3.5−x)	1.01 (x)
$CH_3NH_3BiI_{3-x}Cl_x$	3.34 (1)	0.91 (1)	...	1 (1)	2.47 (4−x)	1.47 (x)
$CH_3NH_3BiI_x$ (1:1)	2.76 (1)	0.30 (1)	...	1 (1)	3.43 (4)	...
$CH_3NH_3BiI_x$ (3:1)	4.70 (3)	1.71 (3)	...	1 (1)	4.27 (6)	...

EDS data for $CH_3NH_3BiI_{3-x}Cl_x$ indicates a halide ratio of approximately 2.5:1.5I:Cl, however this result masks important local variations that will be discussed later. In line with the choice of starting precursor stoichiometries, $CH_3NH_3BiI_3$ (3:1) shows the highest concentration of iodine. Although carbon was found to exist in a 1:1 ratio with nitrogen during elemental analysis of MAI, its relative concentration in each film is increased. We attribute this enhanced carbon content to a combination of sample contamination by carbon caused by electron beam exposure in the SEM and residual levels of trapped solvent.

To identify the origin(s) for the different crystal structures present in the mixed Pb/Bi perovskite films, we note that EDS maps show a generally homogenous distribution of these specific elements throughout each sample. Cl and I are also similarly distributed in both the large and small structures. In contrast, from Fig. 3 noticeable differences in the distribution of the halides in the $CH_3NH_3BiI_{3-x}Cl_x$ film are determined, where I closely maps to the large flower shaped structures present and Cl maps to the thin layer than lies beneath. It appears therefore that in these films there are two different stoichiometries which we subsequently refer to as I-rich and Cl-rich. To determine their molar ratio in each region we conducted a series of point EDS chemical surveys.

As summarized in Table II, in the I-rich regions bismuth preferentially binds to iodine when forming crystalline structures. Unlike in the lead-halide perovskite, a significant amount of chlorine is present in the film, suggesting that its removal during perovskite formation is less efficient when bismuth is present. In the I-rich regions the Bi:Cl:I ratio 1:0.67:2.67. Within the Cl-rich regions the Bi:Cl:I ratio is 1:1.37:1.64. These ratios indicate that the bismuth to halide ratio in both cases is almost 1:3, as one would expect for an ABX_3 perovskite.

TABLE II. The EDS point analysis for the $CH_3NH_3BiI_xCl_y$ film highlighting the distribution of iodine and chlorine rich regions areas.

Materials	C	N	Bi	I	Cl
I-rich region	2.02	0.71	1	2.67	0.67
Cl-rich region	2.57	0.97	1	1.64	1.37

C. GIWAXS characterization

Given the difference in ionic radii for lead, bismuth, chlorine, and iodine, we suggest that the various structures imaged using SEM will also have different crystal lattice parameters. To test this hypothesis, and to also verify the presence of crystallites with a perovskite unit cell structure, samples were measured using GIWAXS. Radially integrated 1D X-ray scattering patterns from each sample are shown in Fig. 4, alongside patterns from films prepared using the precursor materials MAI, $BiCl_3$, and BiI_3. Immediately it can be seen that the diffraction pattern of each perovskite is not a simple linear combination of its precursor ingredients, thereby confirming the precursor components have combined to form new crystalline phases. The GIWAXS data for $CH_3NH_3BiI_{3-x}Cl_x$ shown in Fig. 4(a) demonstrates minimal evidence for X-ray scattering from MAI and $BiCl_3$, supporting the idea that the perovskite has a stoichiometry close to its target value. Nevertheless the presence of X-ray scattering peaks other than those attributable to the perovskite suggests more than one crystalline phase has been formed. For $CH_3NH_3BiI_3$ (1:1) and $CH_3NH_3BiI_3$ (3:1), there are clear indications that unreacted BiI_3 is present within the film as well as unreacted MAI. This result implies that for these blends the precursors do not undergo complete conversion possibly because they are not stoichiometrically well matched. Despite the different mixing ratios used the X-ray scatter pattern from both these new crystal phases are very similar. This is in stark contrast to the different structures observed using SEM (see Fig. 3), demonstrating a strong sensitivity of sample microstructure to precursor composition. This sensitivity to composition has been noted by others.[21,27]

The X-ray scattering from $CH_3NH_3PbI_{3-x}Cl_x$ is similar to previously published data,[21,30,31] allowing us attribute the scattering peaks at $q = 0.99$ to 1.00 $Å^{-1}$, $q = 1.41$ to 1.42 $Å^{-1}$, and $q = 1.99$ to 2.00 $Å^{-1}$ to X-ray scatter from the (002) and (110), (112) and (200), and (004) and (220)

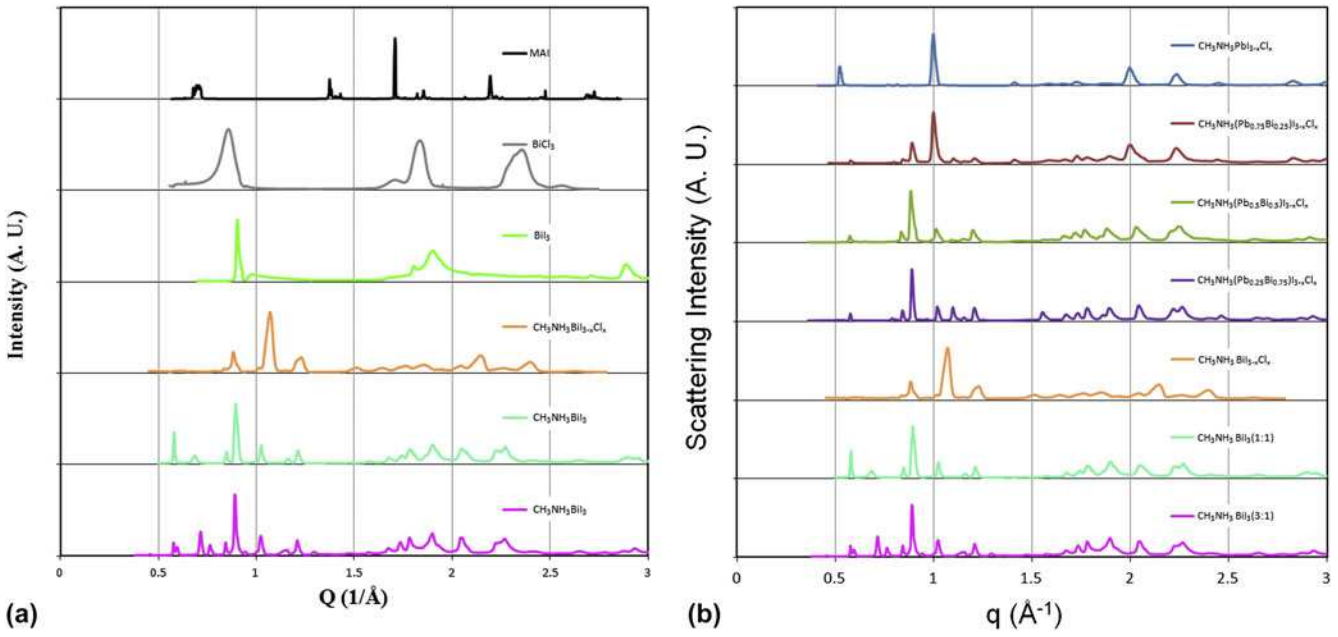

FIG. 4. The 1D radially integrated GIWAXS patterns of $CH_3NH_3PbI_{3-x}Cl_x$, $CH_3NH_3(Pb_{0.75}Bi_{0.25})I_{3-x}Cl_x$, $CH_3NH_3(Pb_{0.5}Bi_{0.5})I_{3-x}Cl_x$, $CH_3NH_3(Pb_{0.25}Bi_{0.75})I_{3-x}Cl_x$, $CH_3NH_3BiI_{3-x}Cl_x$, $CH_3NH_3BiI_3$ (1:1), and $CH_3NH_3BiI_3$ (3:1) films prepared on silicon substrates. (color online)

features of tetragonal $CH_3NH_3PbI_{3-x}Cl_x$ respectively. For this system the corresponding lattice parameters are $a = b = 8.85$ Å and $c = 12.69$ Å, close to the values reported for the pure tri-iodide perovskite.[32–34] The GIWAXS pattern for $CH_3NH_3(Pb_{0.75}Bi_{0.25})I_{3-x}Cl_x$ is broadly similar to $CH_3NH_3PbI_{3-x}Cl_x$, albeit with the addition of new scattering peaks at $q = 0.89$ Å^{-1}, $q = 1.21$ Å^{-1} and peaks of relatively weak intensity between 1.50 Å^{-1} and 2.00 Å^{-1}. This is consistent with the UV–Vis data presented in Fig. 1 that indicated a similar absorption onset for the two samples. For $CH_3NH_3(Pb_{0.5}Bi_{0.5})I_{3-x}Cl_x$, the relative intensity of the peaks at 0.89 Å^{-1} and 1.21 Å^{-1} is higher, however the peaks corresponding to the (110) and (220) reflections from $CH_3NH_3PbI_{3-x}Cl_x$ are found to undergo both a reduction in relative intensity alongside a small shift (c. 1%) to higher q values. This not only implies a reduction in Pb-rich perovskite content within the sample, consistent with the sample preparation conditions and UV–Vis/EDS data discussed earlier, but also a contraction in the unit cell size that may result from compressive strain. Further reductions in Pb content within the sample (i.e., $CH_3NH_3(Pb_{0.25}Bi_{0.75})I_{3-x}Cl_x$), results in an X-ray scattering pattern that is consistent with the observed trend.

In agreement with the SEM data presented in Fig. 2, the presence of X-ray scattering peaks that can be partly attributed to $CH_3NH_3PbI_{3-x}Cl_x$ in the mixed metal samples suggests the formation of distinct crystal phases rather than the formation of an alloy. We suggest that prior to mixing precursor solutions for $CH_3NH_3PbI_{3-x}Cl_x$ and $CH_3NH_3BiI_{3-x}Cl_x$, the partial formation of metal halide complexes has already taken place that favors the eventual formation of crystals containing either (but not both) metals. Interestingly, the observed peaks in the $CH_3NH_3PbI_{3-x}Cl_x$ GIWAXS pattern at 0.89 Å^{-1} and 1.90 Å^{-1} match those from BiI_3, despite the fact that BiI_3 was not present as precursor material. It appears therefore that for these mixed Pb/Bi samples significant halide ion exchange has taken place during sample processing that results in the formation of BiI_3. Furthermore, from Fig. 4(b) it can also be seen that the mixed Pb/Bi samples follow a trend that more closely resembles a transition from $CH_3NH_3PbI_3$ to $CH_3NH_3BiI_3$, rather than to $CH_3NH_3BiI_{3-x}Cl_x$, even though the precursors for $CH_3NH_3BiI_{3-x}Cl_x$ were used for mixing, further indicating that halide exchange occurs.[35]

To better understand the origin of each new feature observed in our GIWAXS measurements, X-ray scattering patterns of single phase powder samples were simulated the using CrystalDiffract 6 software package.[36] Crystal structures (.cif files) for $CH_3NH_3PbI_3$ and BiI_3 were taken from a previous report.[34] The $CH_3NH_3PbI_3$ scattering pattern measured was in good agreement with the previously reported structure. Crystal structures for bismuth perovskites have not been widely reported; therefore we started from a generic ABX_3 structure file (A = methylammonium, B = Bi, and X = halide) and iteratively adjusted the lattice parameters until it matched the experimental data. The fitted lattice parameters for $CH_3NH_3BiI_3$ (prepared from both the 1:1 and 3:1 precursor mixtures) correspond to a tetragonal structure. Figure 5 shows the simulated GIWAXS pattern of a perovskite with unit cell dimensions $a = b = 8.67$ Å and $c = 12.41$ Å and a mixture of this simulated pattern

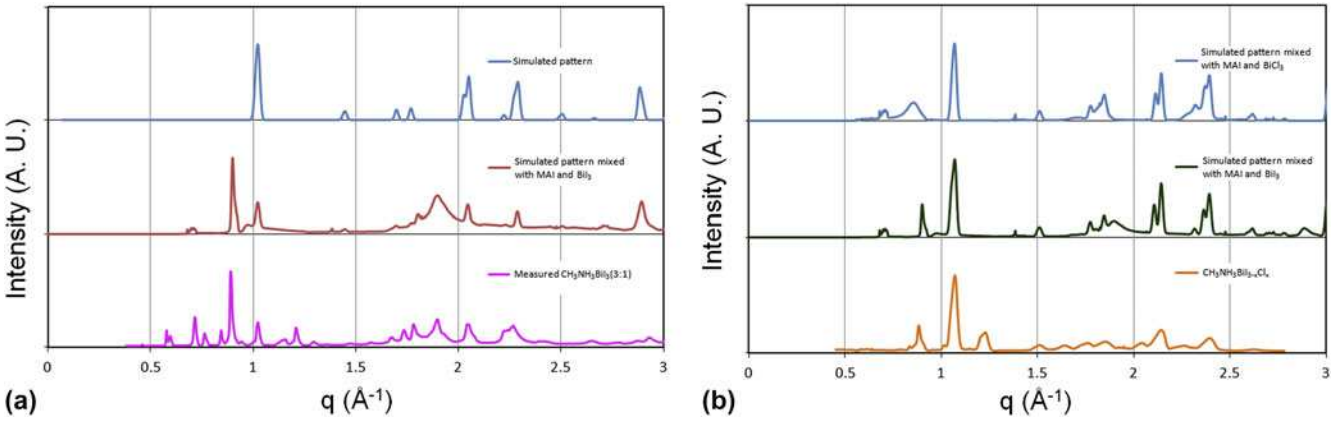

FIG. 5. The GIWAXS patterns from (a) the simulated ABX_3 (tetragonal $a = b = 8.67$ Å and $c = 12.41$ Å), simulated mixture of ABX_3, MAI, and BiI_3, and the experimentally observed pattern from $CH_3NH_3BiI_3$ (3:1) and (b) the simulated ABX_3 (tetragonal $a = b = 8.67$ Å and $c = 12.41$ Å), simulated mixture of ABX_3, MAI, $BiCl_3$, and BiI_3, and the experimentally observed pattern from $CH_3NH_3BiI_{3-x}Cl_x$. (color online)

BiI_3 and MAI. This mixture is compared to the measured data for $CH_3NH_3BiI_3$ and as shown, there is reasonable agreement between the mixture and the experimentally measured data. Specifically, the simulated ABX_3 pattern shows two peaks at the $q = 1.01$ Å^{-1} and 1.02 Å^{-1}, corresponding to the (002) and (110) reflections respectively. The experimental pattern for $CH_3NH_3BiI_3$ also shows a peak at the $q = 1.02$ Å^{-1}, alongside a shoulder at $q = 1.01$ Å^{-1}.

The mixture and the experimental pattern both show several peaks between $q = 1.5$–2.3 Å^{-1}. Therefore, the relatively intense peaks observed can be modeled using a mixture of a generic ABX_3 crystal lattice, MAI and BiI_3, allowing us to conclude that $CH_3NH_3BiI_3$ forms a perovskite structure. However, between $q = 0.5$ Å^{-1} and 1 Å^{-1} there are several weak features that cannot be readily identified, alongside a peak showed at $q = 1.21$ Å^{-1} that is present in the GIWAXS data for every bismuth containing perovskite. These features are tentatively attributed to the presence of unreacted $BiCl_3$ and other impurities.

We also adapted our model to simulate the X-ray scattering pattern for $CH_3NH_3BiI_{3-x}Cl_x$, based on a generic ABX_3 structure, and combined it with data for MAI, BiI_3, and $BiCl_3$. The results are presented in Fig. 5(b). To match the experimental data the best fit lattice parameters used in the simulated ABX_3 structure were $a = b = 8.29$ Å and $c = 11.89$ Å. Weak X-ray scattering features at $q = 1.21$, 1.64, and 2.04 Å^{-1} were not well matched by our model suggesting the presence of unidentified residual phases that are in addition to the perovskite, MAI, BiI_3 and $BiCl_3$.

D. Solar cell performance

Our measurements on methylammonium bismuth- and methylammonium mixed Pb/Bi-perovskite films have evidenced systems with limited phase purity (relative to our control sample for $CH_3NH_3PbI_{3-x}Cl_x$), in addition to the presence of crystalline structures that have incomplete surface coverage and a range of length-scales. To determine whether such films exhibit any photovoltaic functionality, we fabricated a series of inverted architecture solar cell devices according to the structure ITO/PEDOT:PSS/Perovskite/PCBM/Ca/Al. Light J–V curves and tabulated metrics for each device are shown in Fig. 6 and Table III respectively. Here it can be seen that as expected the control devices based on $CH_3NH_3PbI_{3-x}Cl_x$ exhibited the best solar cell performance by a considerable margin, recording average efficiencies of 8.25% ($J_{SC} = -14.7$ mA/cm^2, $V_{OC} = 0.86$ V, FF = 65.3%). This result is similar to our previous work using the same materials and processing routes.[37] In comparison, and in agreement with Park et al.[19] PCE values for the Bi containing devices were very low. Mixed Pb/Bi perovskite solar cells exhibited J_{SC} and V_{OC} below 0.03 mA/cm^2 and 0.5 V respectively. For the $CH_3NH_3BrI_{3-x}Cl_x$ solar cells [data shown in Fig. 6(b)] a maximum PCE of 0.009% was determined (J_{SC} of -0.03 mA/cm^2, $V_{OC} = 0.78$ V, FF = 44.8%). Although its performance was poor, the J–V curve shows the distinctive shape for a photovoltaic device; furthermore a V_{OC} of 0.78 V was high compared to the other Bi containing perovskite solar cells. Lastly, for $CH_3NH_3BrI_3$, a relatively high J_{SC} of 0.08 mA/cm^2 was measured when the perovskite was prepared from a 1:1 mixture of precursor materials. This was offset however by a low V_{OC} value of 0.22 V. $CH_3NH_3BrI_3$ prepared from a 3:1 precursor mixture did not show any measureable photovoltaic effect.

Despite the disappointing device efficiencies reported for the Bi perovskite solar cells it is still noteworthy that these materials can produce a measurable photovoltaic effect. From our SEM, EDS, and GIWAXS data some of

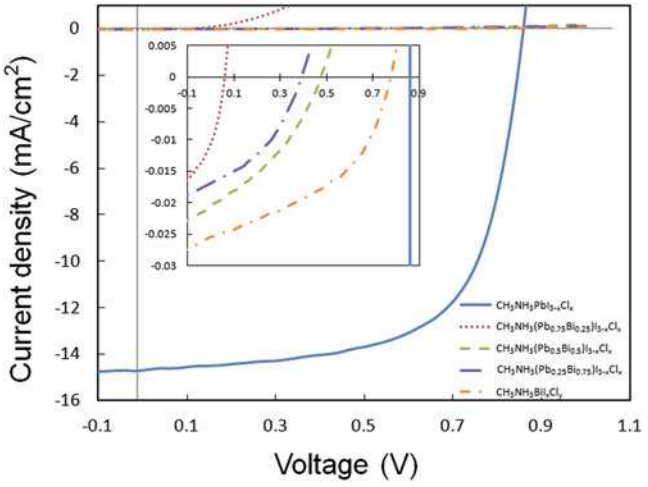

FIG. 6. *J–V* curves for solar cell devices based on $CH_3NH_3PbI_{3-x}Cl_x$, $CH_3NH_3(Pb_{0.25}Bi_{0.75})I_{3-x}Cl_x$, $CH_3NH_3(Pb_{0.5}Bi_{0.5})I_{3-x}Cl_x$, $CH_3NH_3(Pb_{0.75}Bi_{0.25})I_{3-x}Cl_x$, and $CH_3NH_3BiI_{3-x}Cl_x$. (color online)

TABLE III. Photovoltaic performance parameters of the devices produced for this study.

Materials	J_{SC} (mA/cm^2)	V_{OC} (V)	FF (%)	PCE (%)
$CH_3NH_3PbI_xCl_y$	−14.7	0.86	65.3	8.25
$CH_3NH_3Pb_{0.75}Bi_{0.25}I_{3-x}Cl_x$	−0.01	0.06	31.1	0
$CH_3NH_3Pb_{0.5}Bi_{0.5}I_{3-x}Cl_x$	−0.02	0.47	35.9	0.003
$CH_3NH_3Pb_{0.25}Bi_{0.75}I_{3-x}Cl_x$	−0.02	0.39	39.4	0.003
$CH_3NH_3BiI_{3-x}Cl_x$	−0.03	0.78	44.9	0.009
$CH_3NH_3BiI_x$ (1:1)	−0.08	0.22	29.3	0.005
$CH_3NH_3BiI_x$ (3:1)	N/A	N/A	N/A	N/A

the reasons why the performance of these devices are poor can be understood. The material characterization data suggests that both the mixed Pb/Bi and the 100% bismuth based perovskite films contain a significant amount of impurity phases from compounds including BiI_3 and MAI. It is assumed that these are responsible for the dramatically reduced J_{SC}, V_{OC}, and FF values relative to our control device as they may act to increase the internal resistance of the devices. In addition, the inhomogeneous surface coverage of these perovskites will also limit photocurrent efficiency due a reduced effective active area. Given the promising V_{OC} value for $CH_3NH_3BrI_{3-x}Cl_x$, we believe sufficient incentive exists to continue our studies into this material with a focus on the optimization of the semiconductor phase purity and microstructure. By eliminating impurities from the material as well as maximizing its coverage on a substrate layer (potentially via a refined precursor conversion process), it should be possible to realize hybrid perovskite solar cells with improved quantum efficiencies and PCEs, thereby providing a potential low-toxicity alternative to lead-based perovskites for solar cell applications.

III. CONCLUSIONS

In this work, we studied bismuth as a substitute metal cation for lead in hybrid perovskite semiconductors. We show that significant halide ion exchange takes place during sample processing and conclude that $CH_3NH_3BiI_3$ and $CH_3NH_3BiI_{3-x}Cl_x$ adopt a tetragonal perovskite structure with unit cell parameters $a = b = 8.67$ Å and $c = 12.41$ Å and $a = b = 8.29$ Å and $c = 11.89$ Å respectively. Composition and structural analysis of these perovskites evidence the presence of large (>20 μm lateral size) crystallites, alongside regions of smaller crystallites and apparently amorphous material. GIWAXS measurements confirm the inhomogeneous phase composition of these samples, which in combination with their poor surface coverage provides a clear explanation for their inefficient photovoltaic behavior in a solar cell device. The promising V_{OC} for $CH_3NH_3BrI_{3-x}Cl_x$ solar cells (0.78 V) however suggests that efficient solar cells can be realized, with optimization of the perovskite precursor conversion process being an obvious focus for future studies.

IV. EXPERIMENTAL METHODS

A. Material preparation

Perovskite precursors were made from methylamine (33 wt% in ethanol, Sigma–Aldrich Company Ltd.), hydriodic acid (57 wt% in water, Acros Organics), $PbCl_2$ (Acros Organics), BiI_3 (Sigma–Aldrich Company Ltd.), $BiCl_3$ (Acros Organics), and anhydrous DMF (Sigma–Aldrich Company Ltd.). These materials were used as purchased without any further purification.

B. Synthesis of methylammonium iodide (MAI)

24 mL of methylamine solution and 10 mL of hydriodic acid were stirred in 100 mL of ethanol for 2 h under nitrogen. The solvent was dried in a vacuum rotary evaporator. Yellow-white solid was formed and then washed with acetone. The product was dried in vacuum oven overnight at 40 °C. The white crystallized powder of methylammonium iodide was successfully produced as determined by elemental analysis. Anal. Calcd for CH_3NH_3I: C, 7.55; H, 3.81; N, 8.8; I, 79.82. Found: C, 7.67; H, 3.63; N, 8.71; I, 79.80. Elemental analysis was performed using a Perkin Elmer 2400 series II CHN analyser.

C. Methylammonium lead iodide chloride ($CH_3NH_3PbI_{3-x}Cl_x$) precursor

The procedure used to prepare the lead perovskite precursor solution was previously reported by A.T. Barrows et al. In brief, 419.4 mg of MAI (2.63 mmol)

and 244.6 mg of $PbCl_2$ (0.88 mmol) were dissolved in 1 mL of DMF with a solid concentration of 664 mg/mL.

D. Methylammonium bismuth iodide chloride ($CH_3NH_3BiI_{3-x}Cl_x$) precursor

The $CH_3NH_3BiI_{3-x}Cl_x$ was prepared by dissolving 419.4 mg of MAI (2.63 mmol) and 277.3 mg of $BiCl_3$ (0.88 mmol) in 1 mL of DMF resulting in a total solid concentration of 696.7 mg/mL.

E. Methylammonium bismuth iodide [$CH_3NH_3BiI_3$ (1:1)] precursor

Similarly, the $MABiI_x$ was prepared using 139.8 mg of MAI (0.88 mmol) and 518.6 mg of BiI_3 (0.88 mmol) dissolved in 1 mL of DMF. The resulting total solid concentration was 658.4 mg/mL.

F. Methylammonium bismuth iodide [$CH_3NH_3BiI_3$ (3:1)] precursor

419.4 mg of MAI (2.63 mmol) and 518.6 mg of BiI_3 (0.88 mmol) were dissolved in 1 mL of DMF with a solid concentration of 938 mg/mL.

All precursor solutions were heated to and kept at 70 °C overnight to ensure that any solids were fully dissolved. These were subsequently cooled to room temperature and then filtered (0.45 μm PTFE) before use.

G. Mixed metal methylammonium lead bismuth iodide chloride precursors

Three mixed metal precursor solutions were made by mixing the prepared $CH_3NH_3PbI_{3-x}Cl_x$ and $CH_3NH_3BiI_{3-x}Cl_x$ solutions in different ratios. The $CH_3NH_3Pb_{0.75}Bi_{0.25}I_xCl_y$ was made up of 0.75 mL of $CH_3NH_3PbI_{3-x}Cl_x$ and 0.25 mL of $CH_3NH_3BiI_{3-x}Cl_x$. The $CH_3NH_3Pb_{0.5}Bi_{0.5}I_xCl_y$ was made from 0.50 mL of $CH_3NH_3PbI_{3-x}Cl_x$ and 0.50 mL of $CH_3NH_3BiI_{3-x}Cl_x$. Finally, the $CH_3NH_3Pb_{0.25}Bi_{0.75}I_xCl_y$ was made from 0.25 mL of $CH_3NH_3PbI_{3-x}Cl_x$ and 0.75 mL of $CH_3NH_3BiI_{3-x}Cl_x$.

H. Substrates for thin films

To produce thin solid films from each of the precursor solutions they were spin coated onto a solid substrate. Nominally identical samples were prepared on different types of substrate for the different characterization techniques used. For the SEM, EDS, and GIWAXS characterization approximately 15 × 15 mm pieces of Si wafer were used as the substrates. For the UV–Vis absorption spectroscopy 25 × 25 mm pieces of glass were used. Finally for the device fabrication and testing glass substrates prepatterned with ITO electrodes as purchased from Ossila Ltd. were used.

I. SEM, EDS, and GIWAXS characterization

Pieces of silicon wafers were cleaned with acetone and isopropyl alcohol (IPA) in the ultrasonic bath for 10 min each and then exposed to an oxygen plasma for 10 min to remove any organic residues. The perovskite layer was spin coated on the silicon wafer at 5000 rpm then thermally annealed at 90 °C for 90 min. The films were fabricated in air. SEM images and EDS analysis were obtained using JEOL JSM6010LA microscope (10 kV, AU2 Multi-segment BSED detector). GIWAXS analysis was performed at beamline I07 at the Diamond Light Source (10 keV, Pilatus 2M detector, sample-detector distance of ~40 cm).

J. UV–Vis absorption spectroscopy

Glass substrates were cleaned in Helmanex solution, IPA and deionized water in an ultrasonic bath for 10 min for each rinse respectively. The films were fabricated by spin coating (Laurell WS-400BZ-6NPP/lite) on the glass substrates. The films were thermally annealed at 90 °C for 90 min. UV–Vis absorption spectra were measured using an Ocean Optics USB2000+ spectrometer and DT-MINI-2-GS combined deuterium–halogen light source.

K. Device fabrication and characterization

The planar heterojunction architecture used in this work is a relatively easy and fast way to fabricate perovskite solar cells. The perovskite layer is sandwiched between PEDOT:PSS and fullerene layers which act as hole and electron transporting layers, respectively. An advantage of this system is the relative ease with which the thickness of films produced using spin-coating is controlled. Pre-patterned ITO glass substrates (20 Ω/sq) were purchased from Ossila Ltd. The substrates were washed for 10 min each in Helmanex solution, IPA, and deionized water in an ultrasonic bath to remove any dirt on the ITO substrates. After washing, the substrates are blown dry using clean dry nitrogen. PEDOT:PSS (Heraeus Clevios™ P VP AI 4083, Ossila Ltd.) filtered through a 0.45 μm PVDF filter was then spin-coated at 5000 rpm (ACL = 255) for 30 s on the substrates resulting in a thin film of ~40 nm thickness. The PEDOT:PSS coated ITO substrates were then annealed on a hot plate at 130 °C for 15–30 min. The perovskite precursor was subsequently deposited on top of the PEDOT:PSS layer by spin coating at 5000 rpm for 30 s. A small strip of the perovskite film on the edge of substrates was wiped off with a cotton bud to leave an area of the ITO electrodes exposed for contacting. The perovskite coated films were annealed on a hot plate for 90 min at 90 °C. Phenyl-C_{61}-butyric acid methyl ester (PCBM) solution from Ossila Ltd. (50 mg/mL in chlorobenzene filtered through a 0.45 μm PTFE filter)

was heated to 70 °C for 12 h before use. It was then spin-coated on top of the perovskite layers in an oxygen and moisture free glovebox. Again some of the ITO electrode was exposed by wiping off a strip of the PCBM on the edge of substrates using a cotton bud. Calcium and aluminum were deposited onto the PCBM layer through a mask to form cathodes in a vacuum evaporator. The thicknesses of the calcium and aluminum layers were nominally 5 and 100 nm respectively. The devices were then encapsulated with glass using UV-epoxy (Ossila Ltd.) cured under UV light for 30 min. The current density–voltage (*J–V*) characteristics of devices were measured using a Newport 92251A-1000 solar simulator in ambient conditions under simulated AM 1.5 sunlight at an intensity of 100 mW/cm^2 as determined using an NREL calibrated silicon photovoltaic reference cell. The devices were masked with an aperture (0.025 cm^2) to define the active area during the *J–V* measurement to minimize any edge effects. The PCE was subsequently calculated from the *J–V* data and the known illumination intensity.

Author contributions

Kwak prepared the materials and conducted the SEM and device characterization. Dunbar, Barrows, and Pearson conducted the GIWAXS measurements which were modeled by Kwak. All authors contributed to the understanding and interpretation of the results and were involved in the writing process.

ACKNOWLEDGMENTS

We gratefully acknowledge funding from the EPSRC through research grants EP/M025020/1 “High resolution mapping of performance and degradation mechanisms in printable photovoltaic devices” and EP/J017361/1 “Supergen Supersolar Hub”. We thank Diamond Light Source for access to beamline I07 (SI11676-1) that contributed to the results presented here and we acknowledge Jonathan Rawle and Jonathan Griffin for their assistance during the GIWAXS experiments.

REFERENCES

1. S.E. Shaheen, D.S. Ginley, and G.E. Jabbour: Organic-based photovoltaics: Toward low-cost power generation. *MRS Bull.* **30**(1), 10 (2005).
2. D.Y. Liu and T.L. Kelly: Perovskite solar cells with a planar heterojunction structure prepared using room-temperature solution processing techniques. *Nat. Photonics* **8**(2), 133 (2014).
3. M.Z. Liu, M.B. Johnston, and H.J. Snaith: Efficient planar heterojunction perovskite solar cells by vapour deposition. *Nature* **501**(7467), 395 (2013).
4. J. Burschka, N. Pellet, S.J. Moon, R. Humphry-Baker, P. Gao, M.K. Nazeeruddin, and M. Gratzel: Sequential deposition as a route to high-performance perovskite-sensitized solar cells. *Nature* **499**(7458), 316 (2013).
5. J.M. Ball, M.M. Lee, A. Hey, and H.J. Snaith: Low-temperature processed meso-superstructured to thin-film perovskite solar cells. *Energy Environ. Sci.* **6**(6), 1739 (2013).
6. M.M. Lee, J. Teuscher, T. Miyasaka, T.N. Murakami, and H.J. Snaith: Efficient hybrid solar cells based on meso-superstructured organometal halide perovskites. *Science* **338** (6107), 643 (2012).
7. G.E. Eperon, S.D. Stranks, C. Menelaou, M.B. Johnston, L.M. Herz, and H.J. Snaith: Formamidinium lead trihalide: A broadly tunable perovskite for efficient planar heterojunction solar cells. *Energy Environ. Sci.* **7**(3), 982 (2014).
8. N. Pellet, P. Gao, G. Gregori, T.Y. Yang, M.K. Nazeeruddin, J. Maier, and M. Gratzel: Mixed-organic-cation perovskite photovoltaics for enhanced solar-light harvesting. *Angew. Chem., Int. Ed.* **53**(12), 3151 (2014).
9. S.P. Pang, H. Hu, J.L. Zhang, S.L. Lv, Y.M. Yu, F. Wei, T.S. Qin, H.X. Xu, Z.H. Liu, and G.L. Cui: $NH_2CH{=}NH_2PbI_3$: An alternative organolead iodide perovskite sensitizer for mesoscopic solar cells. *Chem. Mater.* **26**(3), 1485 (2014).
10. J.H. Noh, S.H. Im, J.H. Heo, T.N. Mandal, and S.I. Seok: Chemical management for colorful, efficient, and stable inorganic–organic hybrid nanostructured solar cells. *Nano Lett.* **13**(4), 1764 (2013).
11. N.K. Noel, S.D. Stranks, A. Abate, C. Wehrenfennig, S. Guarnera, A.A. Haghighirad, A. Sadhanala, G.E. Eperon, S.K. Pathak, M.B. Johnston, A. Petrozza, L.M. Herz, and H.J. Snaith: Lead-free organic–inorganic tin halide perovskites for photovoltaic applications. *Energy Environ. Sci.* **7**(9), 3061 (2014).
12. NREL: http://www.nrel.gov/ncpv/images/efficiency_chart.jpg, (National Renewable Energy Laboratory, Golden, CO).
13. P.J. Landrigan: Toxicity of lead at low-dose. *Br. J. Ind. Med.* **46**(9), 593 (1989).
14. G. Flora, D. Gupta, and A. Tiwari: Toxicity of lead: A review with recent updates. *Interdiscip. Toxicol.* **5**(2), 47 (2012).
15. A. Babayigit, A. Ethirajan, M. Muller, and B. Conings: Toxicity of organometal halide perovskite solar cells. *Nat. Mater.* **15**(3), 247 (2016).
16. Y. Ogomi, A. Morita, S. Tsukamoto, T. Saitho, N. Fujikawa, Q. Shen, T. Toyoda, K. Yoshino, S.S. Pandey, T.L. Ma, and S. Hayase: $CH_3NH_3SnxPb_{(1-x)}I_3$ perovskite solar cells covering up to 1060 nm. *J. Phys. Chem. Lett.* **5**(6), 1004 (2014).
17. F. Hao, C.C. Stoumpos, D.H. Cao, R.P.H. Chang, and M.G. Kanatzidis: Lead-free solid-state organic–inorganic halide perovskite solar cells. *Nat. Photonics* **8**(6), 489 (2014).
18. W. Travis, E.N.K. Glover, H. Bronstein, D.O. Scanlon, and R.G. Palgrave: On the application of the tolerance factor to inorganic and hybrid halide perovskites: A revised system. *Chem. Sci.* (2016). AU3
19. B.W. Park, B. Philippe, X.L. Zhang, H. Rensmo, G. Boschloo, and E.M.J. Johansson: Bismuth based hybrid perovskites $A_{(3)}Bi_{(2)}I_{(9)}$ (A: methylammonium or cesium) for solar cell application. *Adv. Mater.* **27**(43), 6806 (2015).
20. A.H. Slavney, T. Hu, A.M. Lindenberg, and H.I. Karunadasa: A bismuth-halide double perovskite with long carrier recombination lifetime for photovoltaic applications. *J. Am. Chem. Soc.* **138**(7), 2138 (2016).
21. S. Colella, E. Mosconi, P. Fedeli, A. Listorti, F. Gazza, F. Orlandi, P. Ferro, T. Besagni, A. Rizzo, G. Calestani, G. Gigli, F. De Angelis, and R. Mosca: $MAPbI_{(3-x)}Cl_x$ mixed halide perovskite for hybrid solar cells: The role of chloride as dopant on the transport and structural properties. *Chem. Mater.* **25**(22), 4613 (2013).
22. S.A. Kulkarni, T. Baikie, P.P. Boix, N. Yantara, N. Mathews, and S. Mhaisalkar: Band-gap tuning of lead halide perovskites using

a sequential deposition process. *J. Mater. Chem. A* **2**(24), 9221 (2014).
23. C. Bi, Y.C. Shao, Y.B. Yuan, Z.G. Xiao, C.G. Wang, Y.L. Gao, and J.S. Huang: Understanding the formation and evolution of interdiffusion grown organolead halide perovskite thin films by thermal annealing. *J. Mater. Chem. A* **2**(43), 18508 (2014).
24. Y. Tian and I.G. Scheblykin: Artifacts in absorption measurements of organometal halide perovskite materials: What are the real spectra? *J. Phys. Chem. Lett.* **6**(17), 3466 (2015).
25. T. Ondarçuhu and J.P. Aimé: *Nanoscale Liquid Interfaces: Wetting, Patterning and Force Microscopy at the Molecular Scale* (Pan Stanford publishing, Singapore, 2013).
26. Y.X. Zhao and K. Zhu: CH_3NH_3Cl-assisted one-step solution growth of $CH_{(3)}NH_{(3)}Pbl_{(3)}$: Structure, charge-carrier dynamics, and photovoltaic properties of perovskite solar cells. *J. Phys. Chem. C* **118**(18), 9412 (2014).
27. H. Yu, F. Wang, F.Y. Xie, W.W. Li, J. Chen, and N. Zhao: The role of chlorine in the formation process of "$CH_3NH_3PbI_{3-x}Cl_{(x)}$" perovskite. *Adv. Funct. Mater.* **24**(45), 7102 (2014).
28. E.L. Unger, A.R. Bowring, C.J. Tassone, V.L. Pool, A. Gold-Parker, R. Cheacharoen, K.H. Stone, E.T. Hoke, M.F. Toney, and M.D. McGehee: Chloride in lead chloride-derived organo-metal halides for perovskite-absorber solar cells. *Chem. Mater.* **26**(24), 7158 (2014).
29. L.Q. Zhang, X.W. Zhang, Z.G. Yin, Q. Jiang, X. Liu, J.H. Meng, Y.J. Zhao, and H.L. Wang: Highly efficient and stable planar heterojunction perovskite solar cells via a low temperature solution process. *J. Mater. Chem. A* **3**(23), 12133 (2015).
30. K.W. Tan, D.T. Moore, M. Saliba, H. Sai, L.A. Estroff, T. Hanrath, H.J. Snaith, and U. Wiesner: Thermally induced structural evolution and performance of mesoporous block copolymer-directed alumina perovskite solar cells. *ACS Nano* **8**(5), 4730 (2014).
31. B.W. Park, B. Philippe, T. Gustafsson, K. Sveinbjornsson, A. Hagfeldt, E.M.J. Johansson, and G. Boschloo: Enhanced crystallinity in organic–inorganic lead halide perovskites on mesoporous TiO_2 via disorder-order phase transition. *Chem. Mater.* **26**(15), 4466 (2014).
32. T. Baikie, Y.N. Fang, J.M. Kadro, M. Schreyer, F.X. Wei, S.G. Mhaisalkar, M. Graetzel, and T.J. White: Synthesis and crystal chemistry of the hybrid perovskite (CH_3NH_3) PbI_3 for solid-state sensitised solar cell applications. *J. Mater. Chem. A* **1**(18), 5628 (2013).
33. J.H. Im, C.R. Lee, J.W. Lee, S.W. Park, and N.G. Park: 6.5% efficient perovskite quantum-dot-sensitized solar cell. *Nanoscale* **3**(10), 4088 (2011).
34. C.C. Stoumpos, C.D. Malliakas, and M.G. Kanatzidis: Semiconducting tin and lead iodide perovskites with organic cations: phase transitions, high mobilities, and near-infrared photoluminescent properties. *Inorg. Chem.* **52**(15), 9019 (2013).
35. S.J. Yoon, K.G. Stamplecoskie, and P.V. Kamat: How lead halide complex chemistry dictates the composition of mixed halide perovskites. *J. Phys. Chem. Lett.* **7**(7), 1368 (2016).
36. CrystalMaker Software Limited: http://www.crystalmaker.com/crystaldiffract/. Centre for Innovation & Enterprise, Oxford University Begbroke Science Park, Woodstock Road Begbroke, Oxfordshire, OX5 1PF UK.
37. A.T. Barrows, A.J. Pearson, C.K. Kwak, A.D.F. Dunbar, A.R. Buckley, and D.G. Lidzey: Efficient planar heterojunction mixed-halide perovskite solar cells deposited via spray-deposition. *Energy Environ. Sci.* **7**(9), 2944 (2014).

Supplementary Material

To view supplementary material for this article, please visit https://doi.org/10.1557/jmr.2016.499.

AUTHOR QUERY – jmr.2016.499

1 Please note that the part figures 'a' and 'b' are given in the artwork but not mentioned in the caption of Figure 4. Please provide an updated caption or confirm that this part of the figure should be deleted.

2 Please provide the manufacturer details (company name, city/state if produced in the US or city/country name if produced outside US) for 'JEOL JSM6010LA microscope, beamline I07 at the Diamond Light Source, Ocean Optics USB2000+ spectrometer'.

3 Please provide the volume number and page range for reference '18'.

EDITOR QUERY – jmr.2016.499

These queries are meant for the Production Editor and Editorial Office only. Authors do not need to answer these queries.

1 Please check whether the edits made to the running head are correct.